

Implementation and performance evaluation of controller signal embedded sensorless speed estimation for wind turbine doubly fed induction generators

Yingzhao Wang^a, Slobodan Đukanović^b, Nur Sarma^c, Siniša Djurović^{d,*}

^a Department of Electrical and Electronic Engineering, University of Manchester, UK

^b Faculty of Electrical Engineering, University of Montenegro, Montenegro

^c Department of Engineering, University of Durham, UK

^d Department of Electrical and Electronic Engineering, University of Manchester, UK

ARTICLE INFO

Keywords:

Doubly fed induction generator
Speed estimation
Parabolic interpolation
Spectral analysis
Controller signals

ABSTRACT

This paper reports a novel sensorless speed estimation method for wind turbine doubly fed induction generators that is highly non-invasive and utilises the readily available generator drive controller signals. A generalised analytic analysis is first presented that allows the assessment, identification and study of the controller signal spectral content needed to allow the establishment of real time speed estimation. An overlapping window parabolic interpolation algorithm is then proposed for tracking the controller signal speed dependent spectral content, with a view to provision of an increased real-time estimation rate. The reported method is implemented on a vector controlled doubly fed induction generator laboratory system and tested in transient operating regimes representative of wind generator application. The test results show that high accuracy high estimation rate is achievable in field application characteristic transient dynamics.

1. Introduction

With the modern power system increasingly integrating more power electronic interfaced elements the research on development of intelligent parameter estimation techniques and those allowing improved and more robust utilisation of system components is increasing in prominence [1,2]. In this respect, sensorless speed estimation (SSE) presents attractive prospects for reduced cost and improved reliability electric drive designs, including those in key renewable applications such as wind turbine (WT) generators. SSE application has received significant research for a wide range of induction machine (IM) conventional applications [3,4], and is of considerable interest in wind generators where improved robustness of operation is highly desirable. The conventionally studied SSE methods generally revolve around two widely accepted approaches: the model-observer based (MOB) methods [3,5] and the spectral search based (SSB) techniques [4–6]. The SSB techniques provide the advantage of reduced estimation sensitivity to knowledge of machine parameters, but typically require access to machine terminal signals for implementation. This study explores the feasibility of an SSB estimation scheme utilising the readily available drive controller signals in widely used WT doubly-fed induction generator (DFIG) systems. This

could allow SSE implementation within existing controller logic capacity with no need for additional sensing and processing cost. The underlying aim of the reported study is to evaluate the implementation requirements and potential performance of such a scheme on a practical laboratory based DFIG system.

The SSE SSB techniques generally operate by identifying and extracting a spectral frequency in the machine electrical signals that has a known relationship to rotor speed. The underlying premise is that the real-time tracking of this frequency can enable direct estimation of the rotor speed [4–6]. The key factors that can challenge and limit the application and performance of SSB SSE schemes are: the ability to identify a suitably prominent and consistent spectral component whose frequency carries information on rotor speed in a clearly defined bandwidth of a given IM's electrical signal, and the efficacy of employed frequency analysis method and accurately tracking the spectral frequency of interest. The SSB SSE techniques have been widely researched in squirrel cage IMs to a much lesser extent in wound rotor induction machines (WRIMs) [5–7]. These predominantly employ the stator current signal slot harmonic tracking for speed estimation, applying different time–frequency analysis techniques for real-time extraction of rotor speed to achieve operative SSE solutions; these however can have

* Corresponding author.

<https://doi.org/10.1016/j.ijepes.2023.108968>

Received 28 June 2022; Received in revised form 22 November 2022; Accepted 9 January 2023

Available online 25 January 2023

0142-0615/© 2023 The Authors. Published by Elsevier Ltd. This is an open access article under the CC BY license (<http://creativecommons.org/licenses/by/4.0/>).

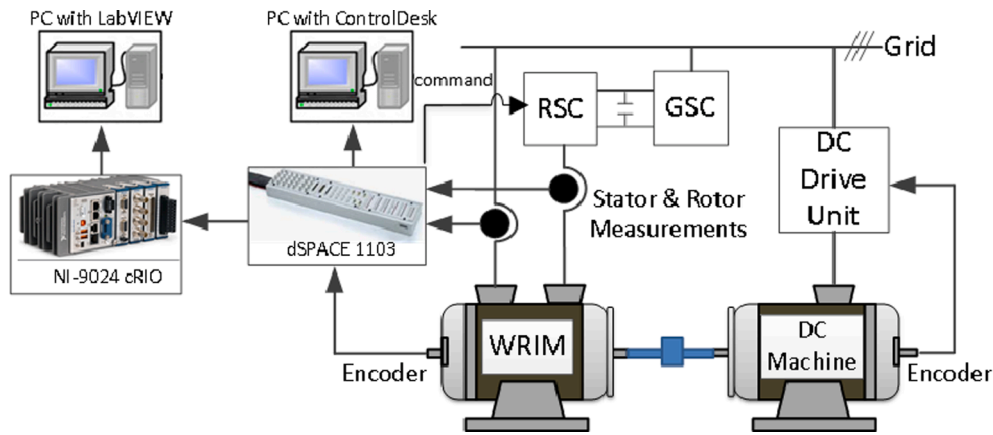


Fig. 1. The simplified schematic diagram of the test-rig.

limitations in the accuracy and dynamics of speed estimation. SSE in WRIMs used in scalar controlled and extended slip applications have been studied in [5,7]. This showed that reasonable efficacy in speed estimation can be obtained from the machine power signal sliding window analysis and the application of a dichotomous search-based time frequency analysis algorithm. The method was found to provide an increased estimation rate with a reduced requirement for system parameters knowledge including the supply frequency.

The application of SSB SSE in vector controlled WRIMs used in modern WT DFIG schemes has received limited research attention. The few reported studies focus on the feasibility of MOB method application that can suffer from pronounced sensitivity to machine parameter knowledge [8,9,10]. Furthermore, the inherently slow dynamics of wind generator systems intrinsically provide good prospects for application of SSB SSE schemes. Attaining an improved robustness sensorless DFIG drive capability would yield potential exploitation and cost reduction advantages in remote and harsh conditions characteristic of WT operation, where encoder failures are not uncommon [11]. To further strengthen the robustness of SSE this work examines the possibility of exploiting the readily available DFIG vector controller signals to establish a SSB speed estimation routine. To this end the paper first presents an analytic study of DFIG controller signals speed dependent spectral contents and their potential to facilitate SSB SSE implementation. A harmonic model of the studied practical DFIG system is then developed, and its results used to characterise the controller signals' spectral contents in a nominal operating speed range and thus verify the analytic study findings. Based on the established understanding a novel controller signal embedded SSB speed estimation algorithm is proposed. The algorithm executes a sliding window spectral search of a DFIG controller signal. Furthermore the algorithm employs the parabolic interpolation time–frequency analysis to provide increased estimation resolution by exploiting inherently low dynamics of wind generator systems. Finally, proposed SSE method has been implemented on a bespoke DFIG laboratory test-rig and its real-time performance assessed and verified in field conditions representative transient experiments.

2. Test-rig description

A vector-controlled laboratory DFIG test-rig was used for experimental investigation of the developed SSB SSE algorithm's performance. The test-rig consists of a 30 kW, four pole, three phase, 50 Hz WRIM, which is mechanically coupled to a 40 kW DC machine prime mover. The DC machine is controlled through a DC drive unit (CT MENTOR – II – M 75R) to regulate the operating speed of the DFIG. The DC machine is set to operate at a desired constant speed or to follow a predefined variable speed-time profile in the experiments.

The stator windings of the WRIM are directly connected to the grid

whereas the rotor windings are connected to a commercial back-to-back converter, comprising two converter units (two CT UNIDRIVE SP-4401, a grid side (GSC) and a rotor side converter (RSC)) that are coupled with a DC link. A stator flux-oriented control (SFOC) scheme was implemented on the RSC using a dedicated real-time routine executed on a dSPACE platform [12,13].

The stator and rotor currents are measured during the experiments using LEM LA 55-P transducers, and the stator voltages using LEM LV25-600 transducers. The rotor speed and position are measured by a 1024 ppr shaft mounted incremental encoder. The outputs of sensors are transferred to the dSPACE platform. The platform is programmed through the Control Desk interface to achieve real-time implementation of the SFOC routine and real-time acquisition of the control loop signals, which are utilised for sensorless speed estimation and the operating speed measurement. The recorded q-axis controller and speed signals are subsequently imported into a NI-9024 cRIO platform to execute the developed SSB SSE algorithm in real-time via the LabVIEW interface and subsequently compare the estimated speed with that measured via the encoder. The LabVIEW interface is also used for data acquisition and signal processing. The signals used in the dSPACE platform real-time control routine are recorded at a sample rate of 5000 Hz. The recorded signals are processed with a 2^{16} points FFT routine in MATLAB, giving a resolution of ~ 0.076 Hz.

Another 1024 ppr incremental encoder is fitted to the DC motor stub shaft to provide speed feedback for the DC drive controller regulating the load. Further details on the test scheme can be found in [12,13]. Fig. 1 shows the simplified schematic diagram of the developed test-rig.

3. Controller signal analysis and sensorless algorithm fundamentals

This section first reviews the general speed dependent spectral contents of the DFIG controller signals of interest. Further analysis is then undertaken, which includes a harmonic model study and analysis of experimental measurements to ascertain the practical behaviour of the controller signals' spectral components.

3.1. DFIG controller signals spectra

The spectral nature of the DFIG's controller signals in a system assumed to contain only the fundamental supply frequency has been assessed in previous research [3]; this work analysed the spectral nature of SFOC signals including those in the inner current controller loops (e.g. d and q axes rotor current demand, rotor current feedback and rotor current error signals) and the outer power controller loops (e.g. stator active and reactive power demand, error and feedback signals). It was shown that the SFOC signals' speed dependent content can be defined

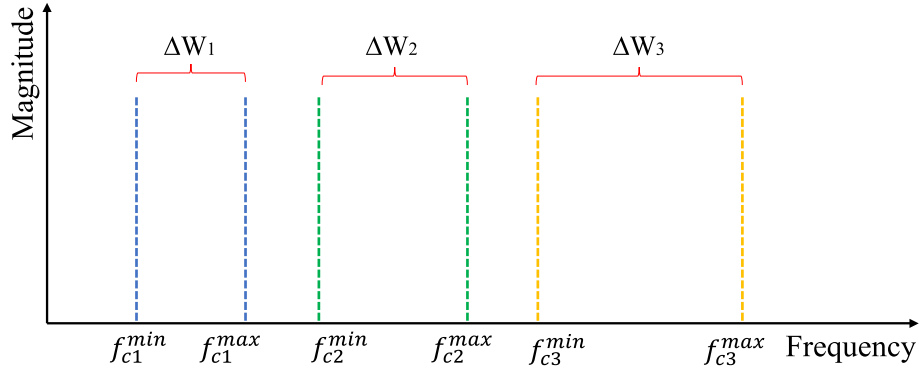


Fig. 2. A general illustration of the controller signal speed dependent spectral content.

with the following analytical expression [5]:

$$f_{ck} = |6k(1 - s)|f \quad (1)$$

In (1): f_{ck} are the possible controller signal spectral component frequencies, k relates to the air-gap field pole numbers ($k = 0, 1, 2, 3, \dots$), s is the slip and f is the supply frequency. Considering the slip definition, i.e.: $s = 1 - n_r / n_s$, where n_r and n_s are the rotor and the synchronous rotational speed in rpm, respectively, and $n_s = 60f / p$, p being the machine pole pair number, allows for expression in (1) to be reformulated to a form that directly links the controller signal k -th harmonic order components' frequency value, f_{ck} , with that of the rotor speed, i.e.:

$$f_{ck} = \frac{kpn_r}{10} \quad (2)$$

(2) clearly illustrates that the SFOC signals can generally be expected to contain a series of harmonics at frequencies equal to integer multiples of $\frac{pn_r}{10}$. Each of these harmonics thus contains information about the rotational speed. Assuming that a given order is manifested at a magnitude level sufficiently prominent to be detectable and its frequency can be accurately extracted and monitored in real-time, an SSE scheme based on monitoring a suitable SFOC embedded signal could in principle be established. To enable this however it is necessary to first characterise and understand the behaviour of the relevant spectral content on a given DFIG system. This would allow an informed decision to be made on identification of a particular controller signal and its spectral content that may be suitable for successful sensorless speed estimation.

A generalised analysis of the expected spectral trends for each controller signal's speed dependent harmonic order can be derived using (2) and the margins of the DFIG operating speed range, commonly accepted to be $\pm 30\%$ around the DFIG synchronous speed [3]. The spectral coordinate of a k -th harmonic order will be centred at its value for DFIG operation at synchronous speed, $f_{Ck}^{synchronous\ speed}$, where $n_r = n_s$, which substituted into (2) gives:

$$f_{Ck}^{synchronous\ speed} = 6kf \quad (3)$$

Depending on whether the DFIG operates in the super-synchronous or the sub-synchronous range (i.e. at rotor speeds higher or lower than the synchronous speed, respectively) the k -th harmonic order spectral coordinate will be correspondingly displaced in the frequency domain. The boundaries of possible spectral displacement can be identified from (2) and the knowledge of the highest (for super-synchronous operation) and lowest (for sub-synchronous operation) operating speed. Assuming the typical highest speed of 30% over synchronous (i.e. $1.3 n_s$ in (2)) gives the following definition of the highest possible frequency taken by a k -th order harmonic, f_{Ck}^{max} , as:

$$f_{Ck}^{max} = 7.8kf \quad (4)$$

In the same manner, the lowest possible frequency value of a k -th order harmonic, f_{Ck}^{min} , can be defined by substituting the lowest DFIG operating speed (i.e. $0.7 n_s$) value in (2) to yield:

$$f_{Ck}^{min} = 4.2kf \quad (5)$$

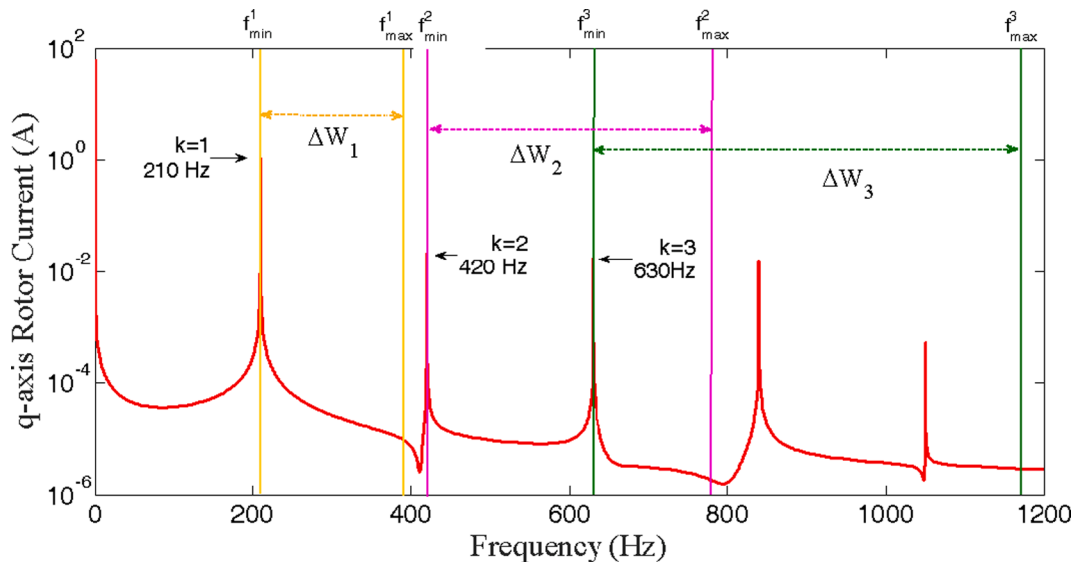


Fig. 3. Predicted I_{qr} spectrum at 1050 rpm, full load.

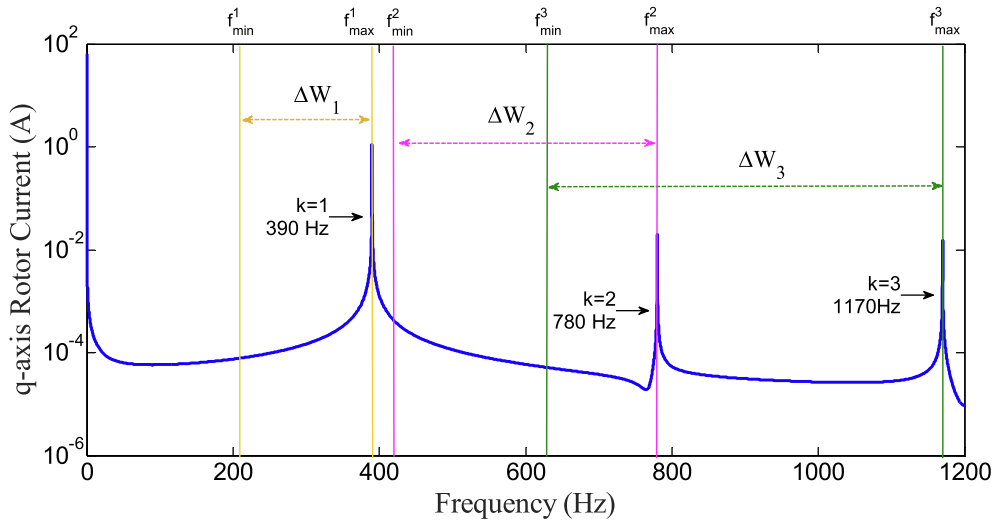


Fig. 4. Predicted I_{qr} spectrum at 1950 rpm, full load.

A general illustration of the controller signal speed dependent spectral content behaviour is illustrated in Fig. 2, showing the possible spectral windows for the first three harmonic orders, bounded by f_{CK}^{min} and f_{CK}^{max} , with a $f_{CK}^{synchronous\ speed}$ centre frequency, that can be inhabited by a given order harmonic component. The general expression for a k -th order spectral window width, ΔW_k containing a k -th order speed dependent harmonic can thus be defined as:

$$\Delta W_k = 3.6kf \tag{6}$$

Spectral analysis confined to a suitable controller signal narrowband and defined using (4) and (5) would in theory allow the isolation of the frequency region occupied by a given order speed harmonic. This would also avoid interference with other non-relevant prominent spectral components that may be present in the wider spectrum. Furthermore, assuming a narrowband can be identified that is maximised by a speed dependent harmonic component, the real-time extraction of this harmonic's frequency would allow real-time information on DFIG operating speed to be attained, and assuming an appropriate time–frequency analysis method can be applied.

The principles put forward in (4) - (6) are further analysed and cross correlated with numerical model and experimental results in the

following section.

3.2. Model and experimental spectral characterisation

A time stepped harmonic model [3] of the test DFIG was employed to map the controller signal's speed dependent contents manifestation in a $\pm 30\%$ slip operating range (i.e. 1050 to 1950 rpm for the test DFIG). The model is based on generalised harmonic analysis and allows representation of the rotational speed dependent spectral content in the DFIG terminal and controller signals [3]. The model is used to examine the spectrum of all SFOC signals. However, for the sake of brevity, the analysis of the q-axis rotor controller current signal, I_{qr} , found to exhibit most prominently the speed dependent harmonic effects of interest on the studied system is presented in this work. The model analysis is validated using corresponding experimental measurements taken on the laboratory test-rig, and those relevant to I_{qr} spectrum analysis shown. For completeness the time domain measurement of the rotor phase and controller currents are shown in Appendix.

The I_{qr} spectral frequency components up to $k = 3$ order are studied as these have been found to be of interest in the test DFIG system examined in this work. The model predicted I_{qr} spectra at lowest (1050

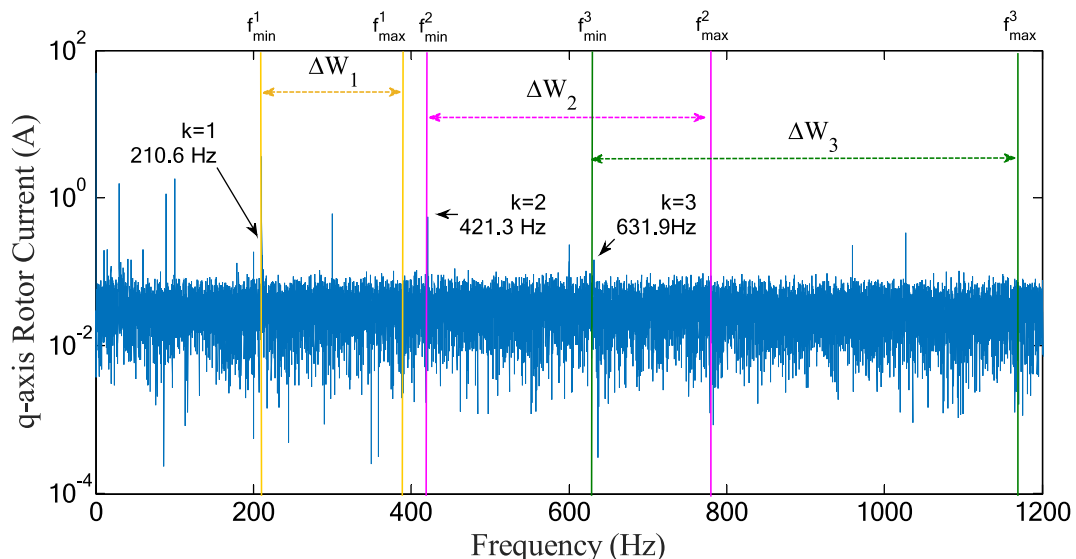


Fig. 5. Practical I_{qr} spectrum at 1050 rpm, full load.

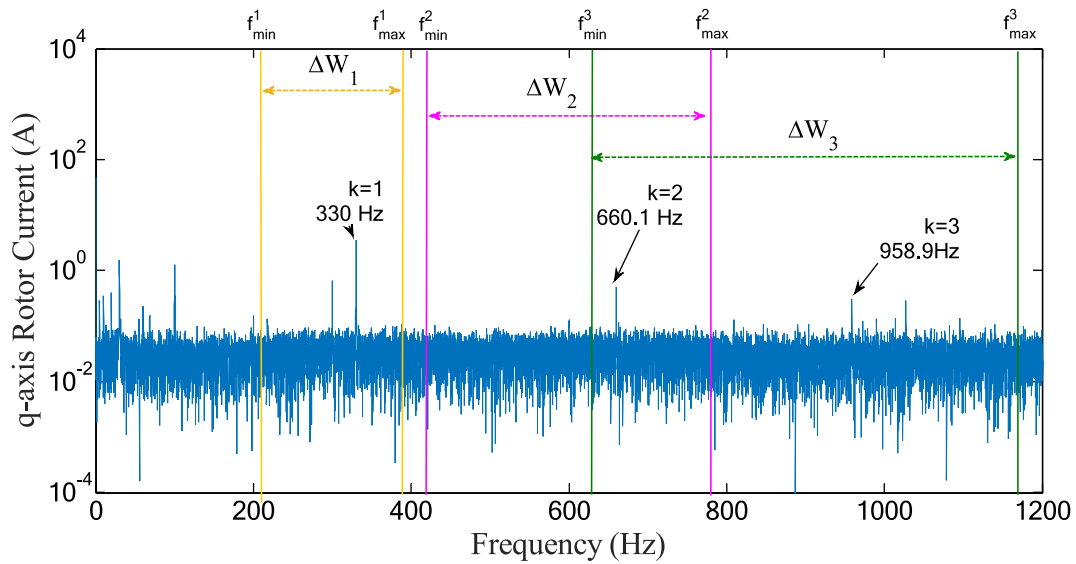


Fig. 6. Practical I_{qr} spectrum at 1650 rpm, full load.

rpm) and highest speed (1950 rpm) in the operating range at full load condition are shown in Figs. 3 and 4, which illustrate the typical spectral content characteristics. This is seen to align with the analysis presented in Section 3.1: the speed dependent harmonic orders given by (2) are evident in the spectra and their predicted lowest and highest numeric values per order for the considered speeds are in agreement with the corresponding spectral components calculated using (4) and (5). Finally, the predicted order window width, ΔW_k , is in agreement with that defined by (6), further validating the analysis in Section 3.1. The presented data suggest that if a suitable spectral window can be monitored that is maximised by a component of a speed dependent frequency, f_{ck} ,

(where $k = 1$ or 2 or 3) then determining that frequency would allow the value of rotational speed to be inferred based on (2). To achieve the frequency determination it is imperative to ensure that the surveyed window is maximised by the speed dependent frequency component [5,6,14]. This however can impose challenges in practical applications where additional spectral content is typically system inherent and can be prominent.

The I_{qr} spectrum was measured in tests in order to experimentally validate the predicted spectra in Figs. 3 and 4. The mechanical integrity limitations on the laboratory test-rig imposed a 1650 rpm maximum speed restriction in tests. The measured I_{qr} spectra at full load and

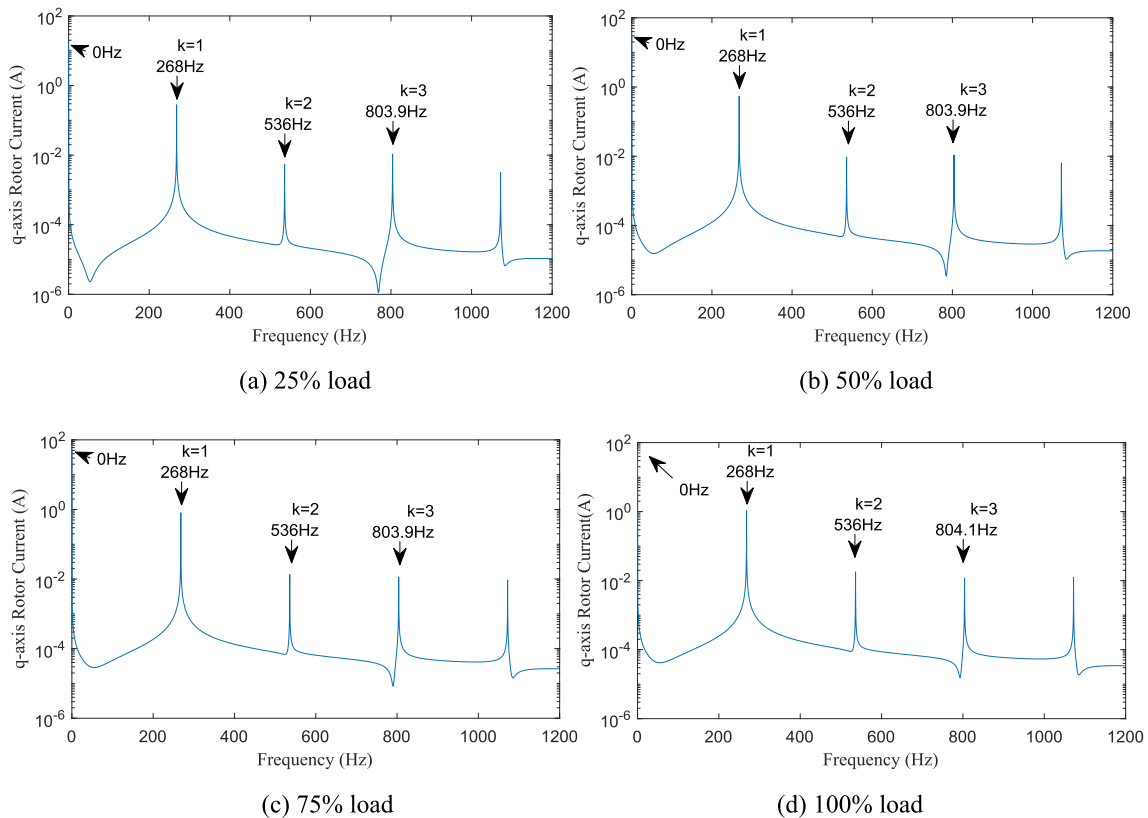


Fig. 7. Predicted I_{qr} spectrum at 1340 rpm, various load conditions.

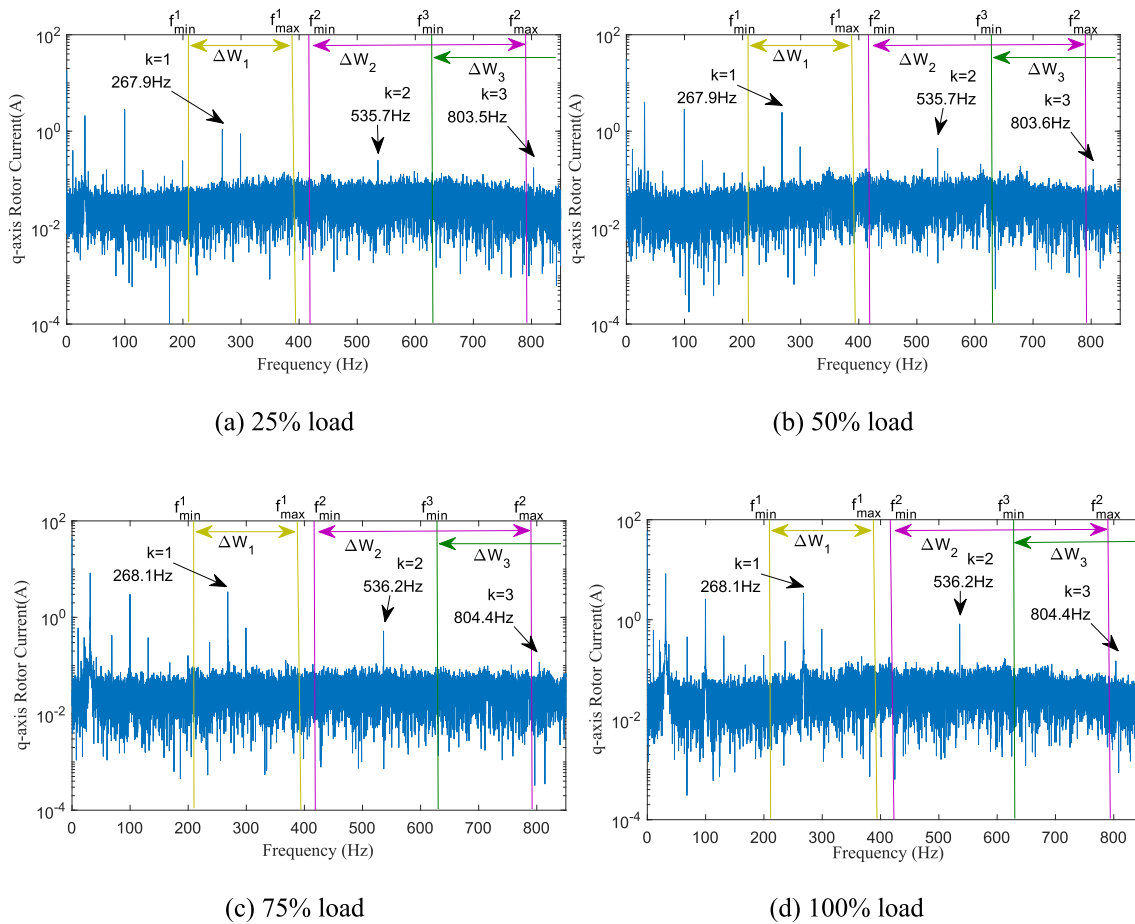


Fig. 8. Practical I_{qr} spectrum at 1340 rpm, various load conditions.

minimum (1050 rpm) and maximum attainable (1650 rpm) speeds on the test system are shown in Figs. 5 and 6, respectively. The speed dependent spectral content was found to agree closely with the model predictions and analysis previously presented in terms of the frequencies of the prominent components: i.e. 210.6 Hz ($k = 1$ in (5)), 421.3 Hz ($k = 2$ in (5)) and 631.9 Hz ($k = 3$ in (5)) in Fig. 5 and 330 Hz ($k = 1$ in (6)), 660.1 Hz ($k = 2$ in (6)) and 958.9 Hz ($k = 3$ in (6)) in Fig. 6. As is generally expected, there are noticeable additional components throughout the spectrum that arise from other system inherent artefacts such as supply harmonics, inverter harmonics and electric unbalances [3,15,20]. These components could in principle endanger the efficacy of SSB based speed estimation if they were prominent in the vicinity of the target spectral components carrying information on rotor speed. It is thus important to observe a spectral window as narrow as possible when attempting frequency tracking: this would in principle ensure minimal interference between the component to be tracked and any undesirable spectral interference.

To further examine the relevant spectral patterns manifestation and potential for detectability under a wider range of relevant operating conditions, the controller loop signals spectrum was predicted in model studies and recorded in experiments, and then analysed in a range of different load levels in the studied operating range (the practically achievable 1050 rpm to 1650 rpm range on the used test system). The 25%, 50%, 75% and 100% load points were assessed while the no load condition is not examined, since WTs are typically energized at moderately low loads and operate to higher loads in service [16].

For illustration purpose and the sake of brevity the relevant I_{qr} spectrum model predictions and corresponding measurements are shown at an arbitrary sub-synchronous operating speed of 1340 rpm in Figs. 7 and 8, respectively. The model predictions indicate consistency of

the spectral content of interest suggesting a generally increasing trend in magnitude with increase in load.

The experimental measurements in Fig. 8 are seen to confirm the trends observed in Fig. 7 model data, which also show an increase in relevant speed dependent frequency component's magnitude with load increase. Among the three observed speed dependent components a strong stator supply unbalance harmonic content (300 Hz) exists near the $k = 1$ content which may affect frequency tracking for SSE, especially in the low load condition. Besides, $k = 3$ content is not as significant in terms of magnitude as the $k = 2$ content. The $k = 2$ component is seen to be prominently displayed in its spectral window, ΔW_2 , where the interference of any surrounding components that may be exhibited at a higher magnitude and thus compromise frequency tracking is seen to be minimal. While most prominently manifested in the spectrum the $k = 1$ component is surrounded by strong secondary spectral content, most evidently at low load, and its frequency tracking through window maximisation could therefore be compromised. The observed spectral phenomena were found to be consistent through the operating spectrum of interest and thus the $k = 2$ component was selected as most suitable for SSE on the practical system used in this work.

4. Sensorless speed estimation algorithm

This section first establishes the fundamental principles of the sensorless speed estimation scheme proposed in this paper. An efficient frequency-domain method used to enable frequency tracking is then introduced and the full sensorless estimation algorithm structure presented.

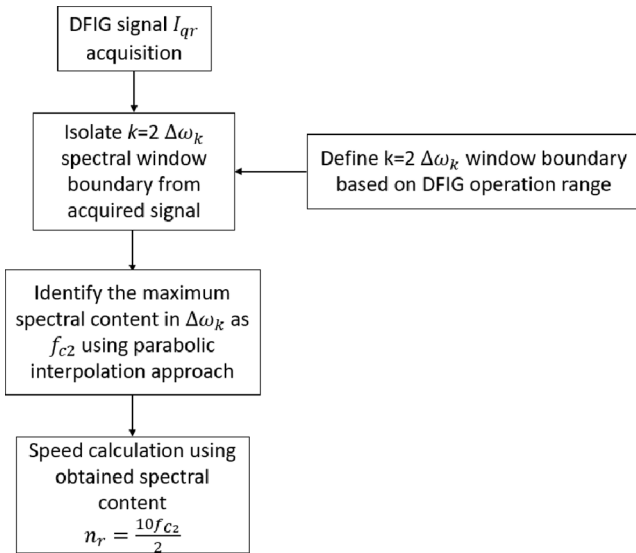


Fig. 9. General structure of the SSB SSE algorithm used in this work.

4.1. Sensorless speed estimation

The controller signal spectral analysis presented in Section 3 indicates that the real-time observation of a spectral window bounded by spectral co-ordinates given by (4) and (5), and of spectral width given by (6), to extract the frequency of the component maximising the spectrum, f_{ck} , could enable the information on DFIG rotor speed to be extracted based on relationship in (2), i.e.:

$$n_r = 10f_{ck}/kp \quad (7)$$

The controller signal study was performed on the examined test system to compare the potential of individual signals to enable SSB speed estimation. It was found that the $k = 2$ order speed dependent spectral component of the q-axis rotor current controller signal, I_{qr} , is optimally suited for SSB speed estimation on the test system used in this work. The general structure of the proposed SSB SSE algorithm is shown in Fig. 9: the procedure involves the isolation of ΔW_2 , i.e. the 2nd order spectral window of I_{qr} and subsequently the real-time extraction of the frequency maximising it, to be used for same time instant evaluation of the rotor speed. The efficacy of the proposed estimator is largely dependent on the spectral analysis method applied for real-time frequency tracking. Due to inherently lower speed dynamics of wind generator systems, this work applies the spectrum maximisation based on the parabolic interpolation technique to achieve frequency tracking, as presented in Section 4.2.

4.2. Spectrum maximisation by parabolic interpolation

The SSB speed estimation performance is defined largely by the efficacy of the applied frequency tracking algorithm. The Discrete Fourier Transform (DFT) is a commonly used tool for spectral analysis. However, FFT is not well suited to real-time dynamic applications including non-stationary signals, where its limitations in estimation accuracy and resolution are significant. To ensure increased estimation rate, while maintaining accuracy, this work employs the parabolic interpolation algorithm [6] for SSB frequency identification, due to its intrinsic features of low computational intensity and high estimation accuracy. The principles of parabolic interpolation application for signal spectrum maximisation are presented in this section.

The periodogram $P(\theta)$ of a discrete signal $x(n)$ (i.e. the DFIG's I_{qr} signal in this work) is defined as:

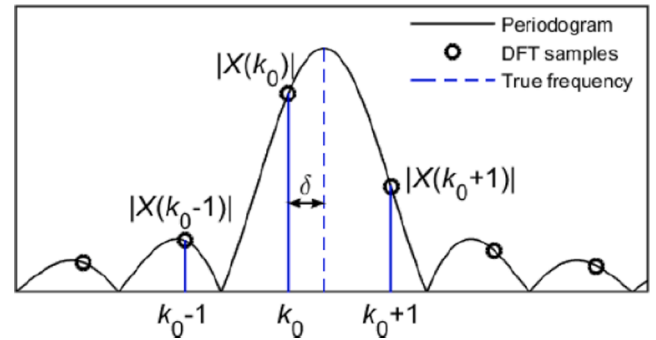


Fig. 10. Illustration of displacement δ of the true frequency from DFT maximum position k_0 [19].

$$P(\theta) = \left| \sum_{n=0}^{N-1} x(n)e^{-j2\pi\theta n} \right| \quad (8)$$

where θ represents the normalised frequency and N is the signal length (number of samples). The periodogram is typically calculated using the DFT. However, the peak of the DFT-based periodogram is generally displaced from the peak of a continuous periodogram (8), as depicted in Fig. 10. The DFT peak is located at a DFT index k_0 , whereas the true maximum frequency is $f = (k_0 + \delta)\Delta f$, where Δf is the frequency resolution¹ [19,21]. The frequency displacement δ meets the condition $-\frac{1}{2} < \delta < \frac{1}{2}$. The DFT maximization is defined as coarse estimation, whereas the estimation of displacement δ is defined as fine frequency estimation [19].

By oversampling the DFT, which can be carried out by zero padding in time domain, the displacement δ can be reduced. However, this approach is limited in performance [14,15] and can be time consuming for lengthy signals. Hence this work proposes to refine the coarse frequency estimation by carrying out parabolic interpolation of the periodogram around the obtained coarse frequency. To that end, two additional periodogram points are introduced, one from each side of the coarse frequency; this yields three equidistant frequencies, $\theta_1, \theta_2, \theta_3$, for which the corresponding periodogram values $P_1 = P(\theta_1), P_2 = P(\theta_2)$ and $P_3 = P(\theta_3)$ are obtained. The frequencies satisfy $\theta_1 = f_c - f_d, \theta_2 = f_c, \theta_3 = f_c + f_d$, where f_c represents the coarse frequency estimate and f_d represents the distance in frequency, which can be selected arbitrarily within the interval $(0, \Delta f/2)$. In [14], $f_d = \Delta f/10$. The points $(\theta_1, P_1), (\theta_2, P_2)$ and (θ_3, P_3) are then fitted by a parabola $A\theta^2 + B\theta + C$, and the position of the parabola maximum, i.e. the abscissa of the parabola's vertex, thus represents the final frequency estimation.

The vector of parabola's coefficients can be expressed as [19]:

$$\begin{pmatrix} A \\ B \\ C \end{pmatrix} = \begin{pmatrix} \theta_1^2 & \theta_1 & 1 \\ \theta_2^2 & \theta_2 & 1 \\ \theta_3^2 & \theta_3 & 1 \end{pmatrix}^{-1} \begin{pmatrix} P_1 \\ P_2 \\ P_3 \end{pmatrix} \quad (9)$$

which results in.

$$A = \frac{\theta_3(P_2 - P_1) + \theta_2(P_1 - P_3) + \theta_1(P_3 - P_2)}{(\theta_1 - \theta_2)(\theta_1 - \theta_3)(\theta_2 - \theta_3)} \quad (10)$$

$$B = \frac{\theta_3^2(P_1 - P_2) + \theta_2^2(P_3 - P_1) + \theta_1^2(P_2 - P_3)}{(\theta_1 - \theta_2)(\theta_1 - \theta_3)(\theta_2 - \theta_3)} \quad (11)$$

$$C = \frac{\theta_2\theta_3(\theta_2 - \theta_3)P_1 + \theta_3\theta_1(\theta_3 - \theta_1)P_2 + \theta_1\theta_2(\theta_1 - \theta_2)P_3}{(\theta_1 - \theta_2)(\theta_1 - \theta_3)(\theta_2 - \theta_3)} \quad (12)$$

¹ Frequency resolution is defined as the distance between two adjacent spectral lines in the DFT spectrum.

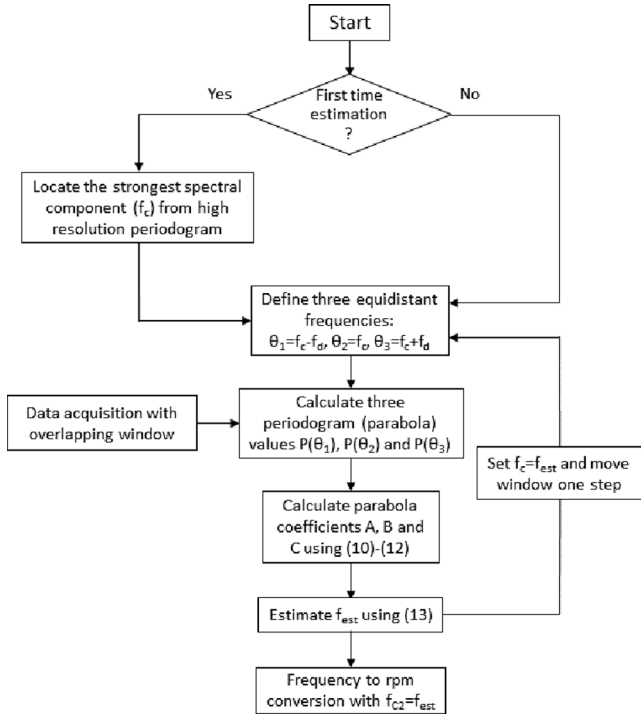


Fig. 11. The complete parabolic interpolation enabled SSB SSE algorithm.

The tracked frequency value, f_{est} (i.e. f_{C2} in Fig. 9 in this work), which corresponds to the abscissa of the parabola vertex, is then given by [14]:

$$f_{est} = -\frac{B}{2A} = -\frac{1}{2} \frac{\theta_3^2(P_1 - P_2) + \theta_2^2(P_3 - P_1) + \theta_1^2(P_2 - P_3)}{\theta_3(P_1 - P_2) + \theta_2(P_3 - P_1) + \theta_1(P_2 - P_3)} \quad (13)$$

The frequency tracking starts with an initial search carried out by maximizing high resolution periodogram, i.e. by locating the maximum of the DFT spectrum of a long signal portion, longer than that used in subsequent frequency tracking steps. The initial frequency estimate is then refined by the proposed parabolic interpolation approach. The frequency tracking then proceeds following the rule: the fine frequency estimate at the current window position is used as the coarse estimate at the next one.

4.3. The complete estimation algorithm

The flowchart of the proposed DFIG SSB SSE algorithm is depicted in Fig. 11. The algorithm steps are detailed as follows:

Step 0: A suitable frequency band of a DFIG signal, maximised by a known speed dependent spectral component, is identified based on analysis presented in Sections 3.1–2.

Step 1: First time fine search: The algorithm begins with an initial high resolution periodogram to obtain the initial high resolution frequency peak location f_c .

Step 2: Calculate three equidistant frequencies: $\theta_1 = f_c - f_d$, $\theta_2 = f_c$ and $\theta_3 = f_c + f_d$, and the corresponding periodogram values $P_1 = P(\theta_1)$, $P_2 = P(\theta_2)$ and $P_3 = P(\theta_3)$. Here, θ_2 is frequency estimation obtained from the first time fine search (Step 1) or from parabolic interpolation (Step 4). The points to be fitted by a parabola are therefore (θ_1, P_1) , (θ_2, P_2) and (θ_3, P_3) .

Step 3: The parabola coefficients A, B and C are calculated using (9)-

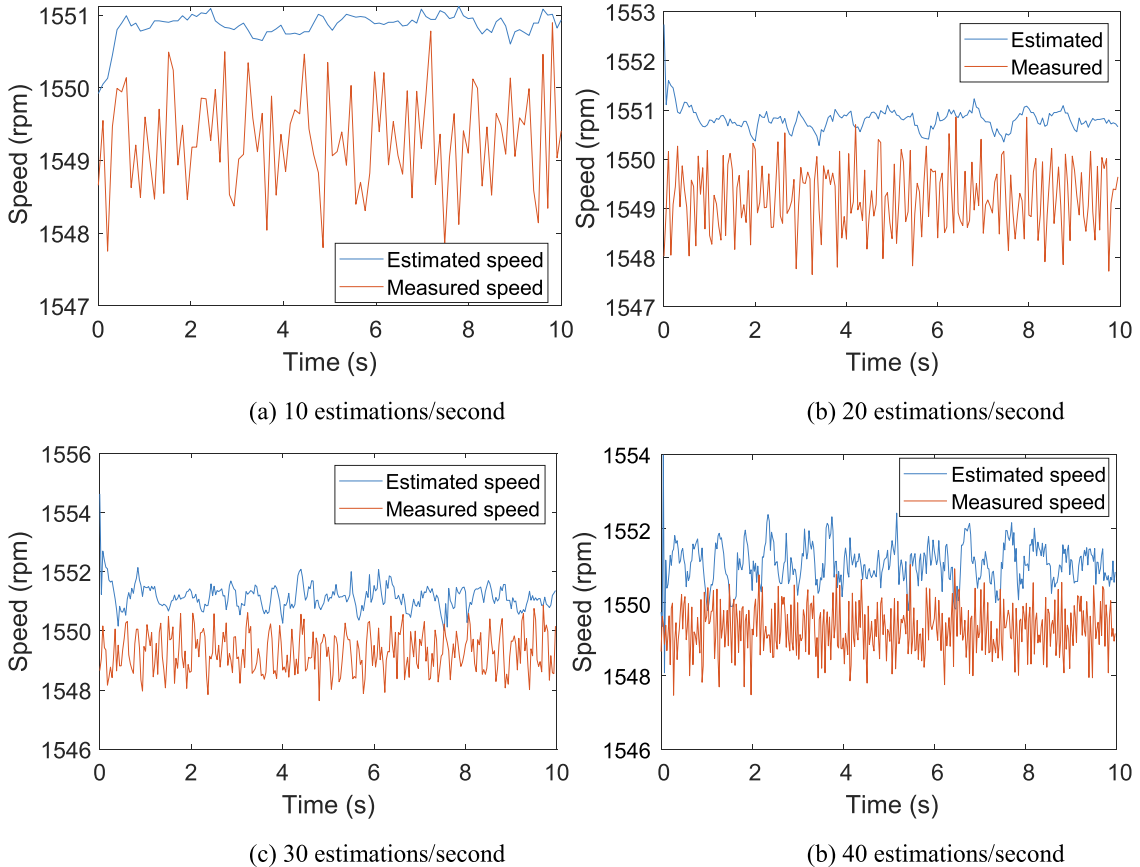


Fig. 12. Real-time speed estimation vs measurement in different estimation rates.

Table 1
Summary of estimation error in different estimation rates.

Estimation rate per second	Sample frequency (Hz)	Max error (%)	Mean error (%)
10	1280	0.21	0.10
20	2560	0.19	0.08
30	3840	0.29	0.12
40	5120	0.38	0.12

(12).

Step 4: Tracked frequency f_{est} , which corresponds to the abscissa of the parabola vertex, is obtained using (13).

Step 5: The machine rotational speed value is obtained from the value of $f_{C2} = f_{est}$ and relation (7).

Step 6: Proceed with analysis of the subsequent data window, while implementing window overlapping. The implementation of overlapping windows is used to increase the estimation rate. Set $f_c = f_{est}$ and go to Step 2.

5. DFIG sensorless speed estimation real-time performance tests

A range of real-time experiments are undertaken in this section to evaluate the efficacy of the proposed algorithm in SSE. Both the DFIG constant speed and field application representative variable speed operation in different load conditions were examined. The rotor speed measured by an encoder mounted on the DFIG shaft was synchronously cross correlated with the estimated speed to ascertain the error rate margins and thus the feasibility and performance potential of the proposed SSE scheme. The findings are presented in the following subsections.

5.1. Constant speed estimation

Speed estimation in steady-state conditions is firstly evaluated to explore the performance of the applied algorithm in a less dynamic set of operating conditions as a precursor to its evaluation in a fully transient generator operating regime. This subsection treats steady state estimation analysis in two stages: first, the evaluation of the algorithm performance at different estimation rates, and then the validation of its performance in a variety of operating load and speed conditions for a fixed estimation rate.

The speed estimation rate is defined as the following, assuming no overlapping window analysis is employed in time–frequency analysis:

$$estimationrate = \frac{f_{sampling}}{n_w} \quad (14)$$

where $f_{sampling}$ is the sampling frequency, n_w is the window size (i.e. the number of data points for each execution). As overlapping window analysis is needed to increase the estimation rate, the estimation rate can be calculated as:

$$estimationrate = \frac{f_{sampling}}{n_w} \times \frac{n_w}{n_s} \quad (15)$$

where n_s is the shift size of window overlap in each algorithm iteration,

Table 2
Summary of estimation error in different load and speed conditions.

1340 rpm			1440 rpm			1550 rpm			1590 rpm		
Load level (%)	Max error (%)	Mean error (%)	Load level (%)	Max error (%)	Mean error (%)	Load level (%)	Max error (%)	Mean error (%)	Load level (%)	Max error (%)	Mean error (%)
25	0.824	0.082	25	0.433	0.078	25	0.368	0.151	25	0.373	0.144
50	0.490	0.077	50	0.277	0.078	50	0.310	0.146	50	0.269	0.139
75	0.300	0.075	75	0.226	0.082	75	0.300	0.143	75	0.249	0.135
100	0.262	0.079	100	0.239	0.080	100	0.283	0.139	100	0.271	0.131

giving:

$$estimationrate = \frac{f_{sampling}}{n_s} \quad (16)$$

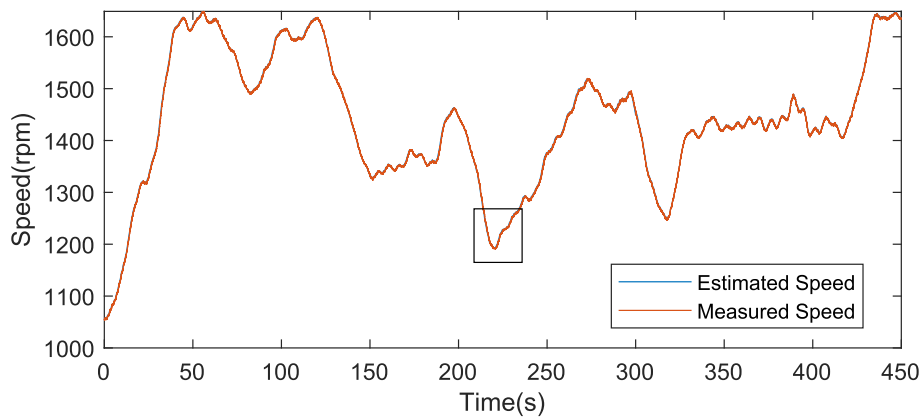
It could be concluded that the estimation rate is theoretically determined by $f_{sampling}$ and n_s . However, in a practical real-time LabVIEW routine, the algorithm execution rate is also limited by the execution window size n_w (i.e. while a larger n_w will yield a higher frequency resolution and thus a more accurate estimate it will also require more time to execute due to an inherent increase in computational demand on the real-time platform). In real-time tests in this work a window size of 2048 samples was applied as it was found to provide optimal computational performance. A window shift size of 128 samples has been applied, which was found to provide a good balance between estimation accuracy and rate in tests.

An evaluation of different estimation rate performance was then undertaken by testing the algorithm operation at a range of different values of f_{sample} . A typical operating point (1550 rpm 100% load) was selected to illustrate the findings of this study. The obtained real-time results for different estimation rates are shown in Fig. 12 and the corresponding error statistics are summarized in Table 1.

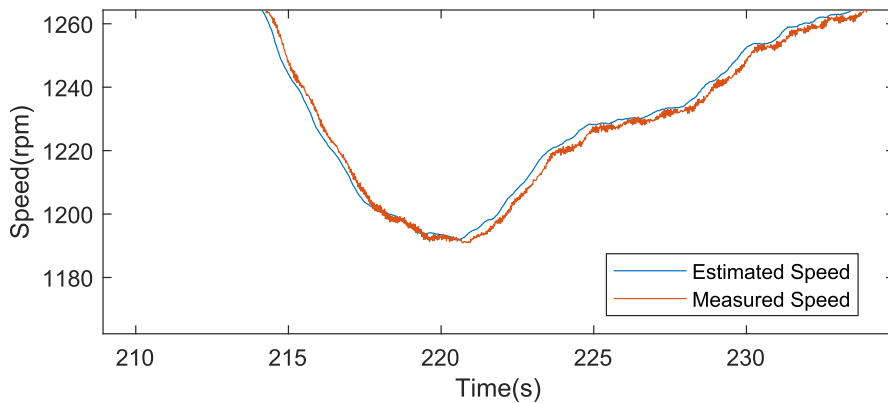
The real-time estimation rate is constrained by the LabVIEW algorithm inherent computing time requirement, which is related to the hardware processor performance and the algorithm programming approach. With the window size of 2048, it takes 24 ms to execute each iteration in the proposed real-time routine, which means the maximum attainable estimation rate with the real time hardware available for this work is approximately 42 estimations per second. In consequence, the estimation rates evaluated in this study range from 10 to 40 estimations per second. Referring to Table 1, the obtained max error rate is in the range of 0.19% to 0.38% whilst the mean error rate is in the range of 0.08% to 0.12%. With the increase of sampling frequency (i.e. estimation rate), the error is slightly increased but a good level of accuracy is maintained. Furthermore, the attained estimation performance parameters provide an improvement compared to that reported in the general SSB SSE literature [7,14,6]. This indicates that the proposed algorithm is competent in real-time estimation at up to 40 estimates per second rate on the available test system but has strong potential for an even higher real time execution rate assuming availability of a more powerful real-time execution platform.

A range of experiments were undertaken to evaluate the algorithm performance in different DFIG operating conditions. The following four operating speeds including two sub- and two super- synchronous points were tested: 1340 rpm, 1440 rpm, 1550 rpm and 1590 rpm. For each considered speed point, four different load levels were examined by performing tests at 25%, 50%, 75% and 100% nominal current load. The estimation rate of 40 per second was selected for these tests. The corresponding error statistics are summarized in Table 2.

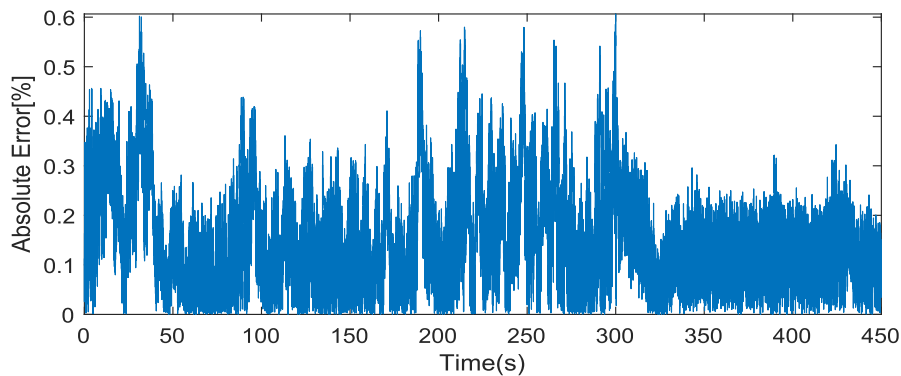
The measurements indicate that the real-time speed estimation can be achieved in both super- and sub- synchronous speed points in all load level conditions: the maximum estimated error rate lower than 0.824% as well as the mean error rate less than 0.151% for low load condition (25%) while the maximum estimated error is lower than 0.49% and the mean error rate less than 0.146% in the load levels $\geq 50\%$. In general, the accuracy of the estimation is seen to increase with the load level



(a) Measured vs estimated speed for wind driven operation



(b) Detailed view of measured vs estimated speed



(c) Instantaneous estimation error

Fig. 13. Measured performance parameters for 100% of load condition.

increase, which is in line with the observations made in Section 3 on speed dependent spectral content magnitude increase with load. Still, the obtained estimation results at low load conditions show a tolerable error rate, with an average error smaller than 0.15% and a maximum error smaller than 0.824%.

5.2. Variable speed estimation

To evaluate the real-time performance for emulated wind-driven operation, an actual wind speed profile was employed at the prime mover side (i.e. DC machine) of the DFIG test system. A transient speed profile in the generating region representative of generator operating dynamics employed in MW size variable speed [2,3,17,18] was used in tests. The transient profile was obtained from a detailed WT model

developed in Supergen Wind Consortium, which was employed to emulate wind resource variation information [5,4]. The employed 450 s speed profile was accommodated to the attainable test system speed range of 1050–1650 rpm for the purpose of this study. As mentioned in Section 5.1 (see Table 1), the sampling frequency was set at 5120 Hz to enable a 40 estimations per second rate, highest allowed by the available FPGA platform computational capacity. For illustration purposes the time domain real-time estimation results obtained for 100% (full load) and 25% load scenarios are shown in Figs. 13 and 14, respectively. In addition, Table 3 shows the measured performance parameters for all the investigated load conditions of this speed profile test.

The results demonstrate that real-time speed estimation is feasible for the operating ranges from sub-synchronous speed to super-synchronous speed of the DFIG in all load conditions. The average

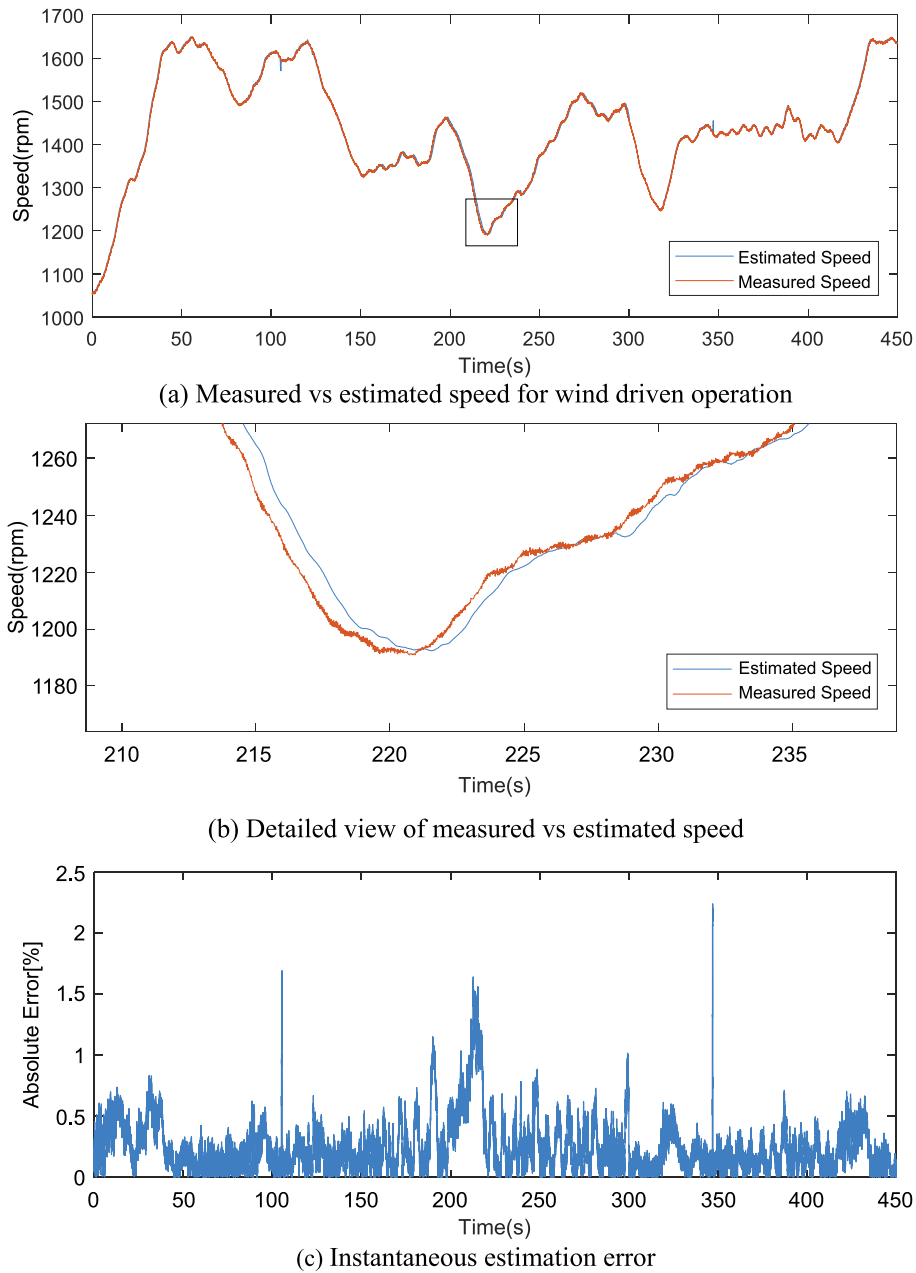


Fig. 14. Measured performance parameters for 25% of load condition.

Table 3
Summary of estimation error in different load conditions.

Load level (%)	Max error (%)	Mean error (%)
25	2.24	0.25
50	1.13	0.23
75	1.10	0.21
100	0.61	0.15

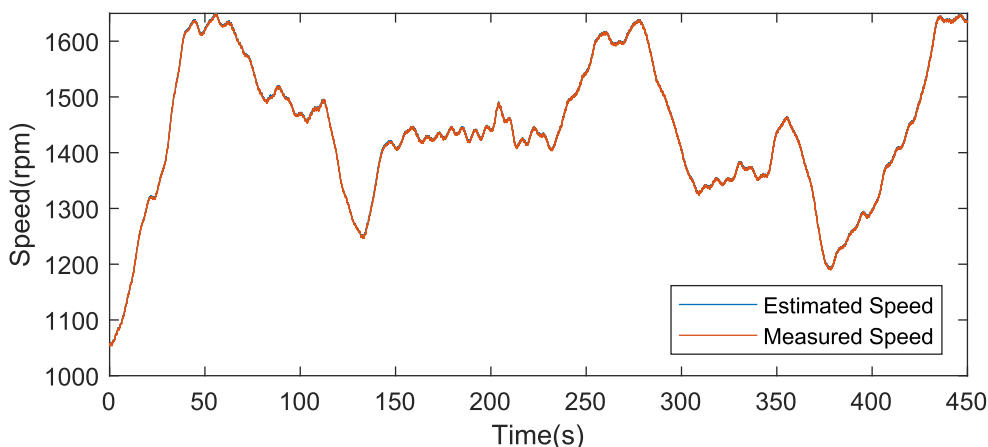
estimation error is lower than 0.25% and maximum error is lower than 2.24% for all load conditions. Similar to constant speed estimation, more accurate estimation could be achieved in higher load conditions (i.e. higher than 50% load in observed tests), as the tracked spectral content is more pronounced in these operating conditions and thus, yields a higher speed estimation consistency. It is also important to point out that transient operation in higher load conditions is more typical of practical wind turbine generators operation, as these are designed to operate in as

high average winds/loads as possible at the given location, hence the good accuracy estimation results at higher loads could be deemed more pertinent to practical, field applications of wind generators.

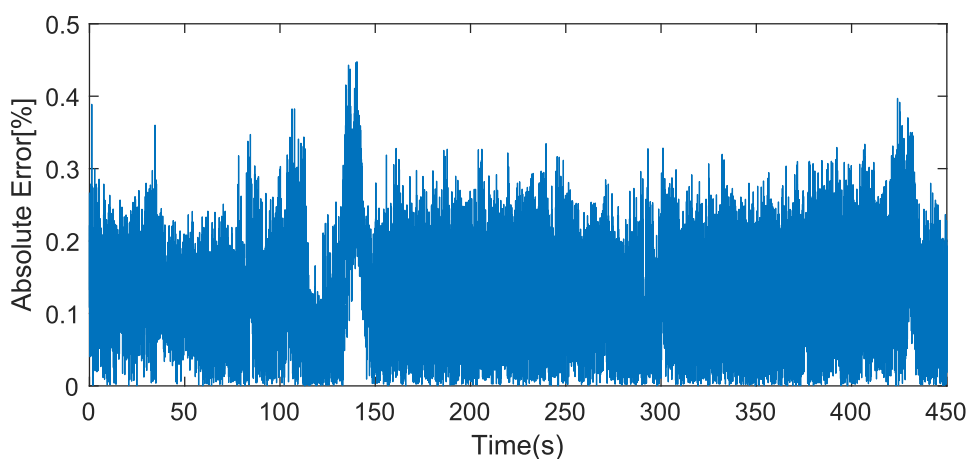
For completeness, another 450 s variable speed profile was also tested in different load conditions. The results obtained at the full load condition are shown in Fig. 15, and the results obtained from other examined cases summarized in Table 4. These results are consistent with the performance levels observed in earlier transient test and further demonstrate the capability of the presented algorithm.

6. Conclusions

This paper reports a new spectral search based speed estimation technique for DFIG drives that utilises the readily available DFIG controller signals. The possible speed dependent spectral content of the controller signals is analytically and experimentally analysed. Furthermore, simple rules for clear definition of possible bandwidths that may



(a) Measured vs estimated speed for wind driven operation



(b) Instantaneous estimation error

Fig. 15. Measured performance parameters for full load condition.

Table 4

Summary of estimation error in second speed profile different load conditions.

Load level (%)	Max error (%)	Mean error (%)
25	1.88	0.26
50	0.92	0.24
75	0.78	0.20
100	0.45	0.13

be maximised with speed dependent spectral components of interest for speed estimation are defined. The proposed sensorless estimation algorithm is underpinned by an effective frequency analysis technique that allows for increased rate estimation while retaining accuracy.

The performance of the reported algorithm has been evaluated in real-time experiments on a purpose devised laboratory DFIG test system. The algorithm was found in tests to provide a high rate high accuracy estimation for all except very low generator loads in both steady-state and, crucially, in field application representative transient operating conditions. The scheme’s performance was found to degrade at very low loads, however these conditions are uncommon in practical DFIG application so would not generally be expected to present a major impediment to potential field application of the proposed technique. The feasibility of the proposed scheme’s implementation in a given system would however be highly dependant on the spectral nature the generator signals, as is typical of SSB SSE schemes.

CRedit authorship contribution statement

Yingzhao Wang: Conceptualization, Methodology, Validation, Visualization, Investigation, Software, Formal analysis, Data curation. **Slobodan Đukanović:** Conceptualization, Methodology, Validation, Visualization, Investigation. **Nur Sarma:** Data curation. **Siniša**

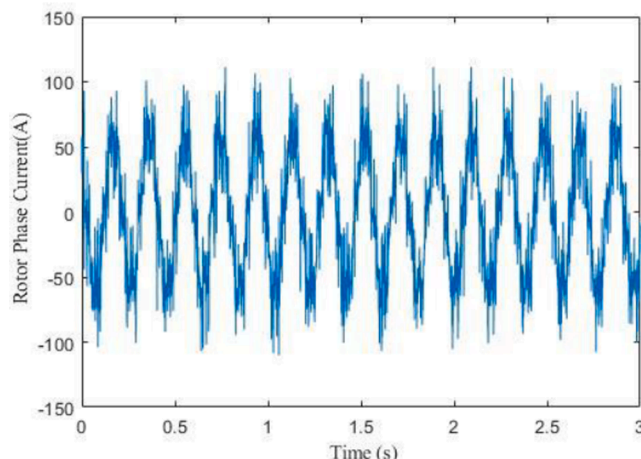


Fig. A1. Rotor phase current signal.

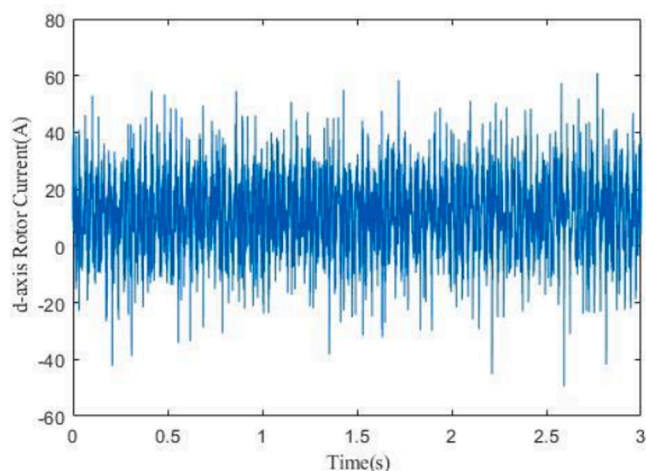


Fig. A2. Rotor d-axis current signal.

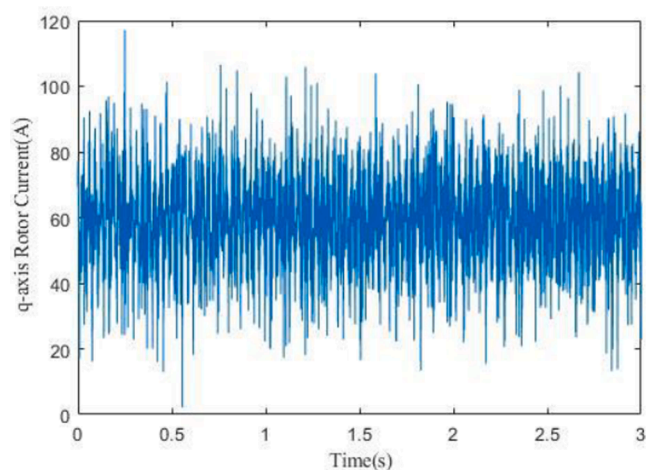


Fig. A3. Rotor q-axis current signal.

Djurović: Supervision, Project administration, Funding acquisition, Formal analysis.

Declaration of Competing Interest

The authors declare that they have no known competing financial interests or personal relationships that could have appeared to influence the work reported in this paper.

Data availability

Data will be made available on request.

Appendix A

The measured time domain rotor phase current signal, and the rotor

controller q and d axes currents for operation at 1340 rpm and full load are shown in Figs. A1-A3 for illustration purposes.

References

- [1] Tan B, Zhao J, Netto M, Krishnan V, Terzija V, Zhang Y. Power system inertia estimation: Review of methods and the impacts of converter-interfaced generations. *Int J Electr Power Energy Syst* 2022;134.
- [2] Xiahou K, Liu Y, Li M, Wu Q. Sensor fault-tolerant control of DFIG based wind energy conversion systems. *Int J Electr Power Energy Syst* 2020;117.
- [3] Ruban Periyannayagam A, Joo Y. Integral sliding mode control for increasing maximum power extraction efficiency of variable-speed wind energy system. *Int J Electr Power Energy Syst* 2022;139.
- [4] Liu Y, Wang Z, Xiong L, Wang J, Jiang X, Bai G, et al. DFIG wind turbine sliding mode control with exponential reaching law under variable wind speed. *Int J Electr Power Energy Syst* 2018;96:253–60.
- [5] Sarma N, Tuohy P, Djurović S. Modelling, analysis and validation of controller signal interharmonic effects in DFIG Drives. *IEEE Trans Sustain Energy* 2019;11(2): 713–25.
- [6] Yang W, Tavner P, Crabtree CJ. Cost-effective condition monitoring for wind turbines. *IEEE Trans Ind Electron* 2010;57(1):263–71.
- [7] Tshiloz K, Vilchis-Rodriguez D, Djukanović S, Sarma N, Djurović S. Sensorless speed estimation in wound rotor induction machines by spectral search of the stator phase power signal. *IET Electr Power Appl* 2016;10(6):581–92.
- [8] Hurst K, Habetler T. Sensorless speed measurement using current harmonic spectral estimation in induction machine drives. *IEEE Trans Power Electron* 11(1) (1996).
- [9] Tshiloz K, Djurović S. Scalar controlled induction motor drive speed estimation by adaptive sliding window search of the power signal. *Int J Electr Power Energy Syst* 2017;91:80–91.
- [10] Mbukani MWK, Gule N. Comparison of high-order and second-order sliding mode observer based estimators for speed sensorless control of rotor-tied DFIG systems. *IET Power Electron* 2019;12(12):3231–41.
- [11] Mondal P, Tripathy P, Saha UK. Second Order Sliding Mode Observer Design for the Speed Estimation of DFIG. 2020 IEEE International Conference on Power Electronics, Drives and Energy Systems (PEDES). 2020.
- [12] Carmeli MS, Castelli-Dezza F, Iacchetti M, Perini R. Effects of mismatched parameters in MRAS sensorless doubly fed induction machine drives. *IEEE Trans Power Electron* 2010;25(11):2842–51.
- [13] Sharpley N. *Windpower Engineering & Development*, 5 2015. [Online]. Available: <https://www.windpowerengineering.com/how-can-you-prevent-encoder-failure-in-wind-turbines/> [Accessed 3 2022].
- [14] Sarma N, Tuohy PM, Apsley JM, Wang Y, Djurović S. DFIG stator flux-oriented control scheme execution for test facilities utilising commercial converters. *IET Renew Power Gener* 2018;12(12):1366–74.
- [15] Sarma N, Apsley JM, Djurović S. Implementation of a conventional DFIG stator flux oriented control scheme using industrial converters. In: 2016 IEEE International Conference on Renewable Energy Research and Applications (ICRERA), Birmingham; 2016.
- [16] Silva W, Lima A, Oliveira A. Speed estimation of an induction motor operating in the nonstationary mode by using rotor slot harmonics. *IEEE Trans Instrum Meas* 2015;64(4):984–94.
- [17] Agrawal S, Mohanty SR, Agarwal V. Harmonics and inter harmonics estimation of DFIG based standalone wind power system by parametric techniques. *Int J Electr Power Energy Syst* 2015;67:52–65.
- [18] Abad G, Lopez J, Rodriguez M, Marroyo L, Iwanski G. *Doubly fed induction machine : modelling and control for wind energy generation*. Wiley-IEEE press; 2011.
- [19] Djukanović S, Popović T, Mitrović A. Precise sinusoid frequency estimation based on parabolic interpolation. In: 24th Telecommunications Forum (TELFOR), Belgrade; 2016.
- [20] Djurovic S, Crabtree CJ, Tavner PJ, Smith AC. Condition monitoring of wind turbine induction generators with rotor electrical asymmetry. *IET Renew Power Gener* 2012;6(4):207–16.
- [21] Djukanović S. Sinusoid frequency estimator with parabolic interpolation of periodogram peak. In: 40th International Conference on Telecommunications and Signal Processing, Barcelona, Spain; 2017.